

Towards Better Surgical Instrument Segmentation in Endoscopic Vision: Multi-Angle Feature Aggregation and Contour Supervision

Fangbo Qin, Shan Lin, Yangming Li, Randall A. Bly, Kris S. Moe, Blake Hannaford*, *Fellow, IEEE*

Abstract—Accurate and real-time surgical instrument segmentation is important in the endoscopic vision of robot-assisted surgery, and significant challenges are posed by frequent instrument-tissue contacts and continuous change of observation perspective. For these challenging tasks more and more deep neural networks (DNN) models are designed in recent years. We are motivated to propose a general embeddable approach to improve these current DNN segmentation models without increasing the model parameter number. Firstly, observing the limited rotation-invariance performance of DNN, we proposed the Multi-Angle Feature Aggregation (MAFA) method, leveraging active image rotation to gain richer visual cues and make the prediction more robust to instrument orientation changes. Secondly, in the end-to-end training stage, the auxiliary contour supervision is utilized to guide the model to learn the boundary awareness, so that the contour shape of segmentation mask is more precise. The effectiveness of the proposed methods is validated with ablation experiments conducted on novel Sinus-Surgery datasets.

I. INTRODUCTION

With the rapid development of surgical robotics, computer-assisted intervention, and computer vision technologies, increasing attention has been paid to how intelligent endoscopic vision can benefit surgery performance and clinical outcome [1]. For example, endoscopic video-based navigation was used for registration in sinus surgery [2], the dense reconstruction of 3D surgical scene was developed for handheld monocular endoscopy [3], the endoscopic video-based augmented reality (AR) could increase surgeon’s visual awareness of high-risk targets [4], and the operative skill assessment was realized based on surgical video [5]. Surgical robots, such as the widely-applied da Vinci systems [6] and the collaborative research platform Raven-II [7], can gain more flexibility and autonomy from endoscopic vision. In [8], real-time endoscopic vision was used to guide

semi-autonomous tumor resection. The real-time 3D tracking of articulated tools helped the safe tool-tissue interaction of da Vinci robot [9]. For the above endoscopic vision perception applications, instrument segmentation, i.e. separating the instrument from the tissue background, is a key technology, providing the essential region information so that we can estimate the instrument position and analyze the instrument and tissue separately.

Surgical scene complexity is usually more limited than natural scenes, which involves only several types of instruments and organs. However, frequent instrument-tissue contacts, non-uniform illumination, deformable reflective surfaces, and continuous change of observation perspective pose many challenges to image segmentation.

A. Related Works

In recent years, deep neural networks (DNNs) have significantly advanced endoscopic image perception [10]. With enough training data, DNNs surpass the traditional hand-crafted feature based methods due to DNN’s feature learning ability and deep hierarchical structure. For real-time instrument segmentation, the lightweight ToolNet models were designed based on holistically-nested structures, and outperformed the classical segmentation model FCN-8s [11, 12]. Laina *et al.* combined the landmark localization and segmentation tasks in one DNN model [13]. The recurrent neural networks layers were embedded within the convolutional model to model the pixel interdependencies [14]. In [15], the ToolNet-C model was a cascade of a feature extractor and a segmentor, which were trained on numerous unlabeled images and a few labeled images, respectively. U-net is a classical architecture proposed for biomedical images, which has a symmetric structure and multiple skip connections [16].

Facing more challenging surgical scenes, the DNN-based segmentation requires larger model capability and deeper structure. Shvets *et al.* modified the LinkNet [18] and TernaNet [19] models to LinkNet-34 and TernaNet-16 for instrument segmentation, respectively, between which TernaNet-16 provided the better accuracy. Islam *et al.* proposed a real-time instrument segmentation model with a multi-resolution feature fusion module, which fuses the two high- and low-resolution feature maps given by the main and auxiliary branches, respectively [20]. In the experiments, the proposed multi-resolution method outperformed the general-purpose semantic segmentation models like PSPNet [21] and ICNet [22]. Ni *et al.* designed the LWANet based on a

F. Qin is with Research Center of Precision Sensing and Control, Institute of Automation, Chinese Academy of Sciences, Beijing 100190, China, and School of Artificial Intelligence, University of Chinese Academy of Sciences, Beijing 101408, China. {qinfangbo2013@ia.ac.cn}

S. Lin and B. Hannaford are with Department of Electrical Engineering, University of Washington (UW), Seattle, WA 98195-2500, USA. R. A. Bly, and K. S. Moe are with Department of Otolaryngology-Head & Neck Surgery, UW, Seattle, USA. {corresponding author: blake@uw.edu}

Y. Li is with Department of Electrical Computer and Telecommunications Engineering Technology, Rochester Institute of Technology, USA.

lightweight encoder and channel-attention guided decoder, which achieves real-time speed for large surgical images [23]. It is advantageous to incorporate optical flow based inter-frame motion cues into segmentation [24]. However, the optical flow estimation task could be challenging in endoscopic vision, especially when the illumination and background are highly dynamic.

B. Motivation and Contributions

This paper aims to propose embeddable methods to realize relative accuracy improvement for the current surgical instrument segmentation models. We observe the two problems: 1) Although the random rotation with large-range is usually included in the data augmentation during training, the segmentation could still be sensitive to the instrument orientation's change. In endoscopic surgery scenarios, the endoscope's axial symmetry and the dexterous motion frequently lead to instrument rotation in the endoscopic view. 2) The predicted segmentation masks are prone to have incomplete and inaccurate parts near the instrument boundary. Considering these two problems, our contribution is as follows.

1) The *multi-angle feature aggregation* (MAFA) method is proposed, which can be flexibly incorporated with a DNN segmentation model, without increasing the model's parameter number. The aggregation of visual features augmented by multi-angle rotation provides better robustness and accuracy.

2) The *contour supervision* is utilized as an auxiliary learning task in the training stage, which guide the model to learn features highly related to instrument boundary, so that the prediction near the boundary can be refined.

3) The novel *Sinus-Surgery datasets* (online available¹) were collected from multiple endoscopic sinus surgery processes conducted by surgeons, which are featured by dexterous tip motion, narrow operation space and close lens-object distance.

II. METHODS

A. Semantic Consistency under Rotation-and-Alignment

For endoscopic images, we assume the semantic consistency under rotation-and-alignment. The *rotation* operation is to rotate a map with an angle around the image center, and the *alignment* operation is to rotate the map with the same angle but in the reversed direction. Intuitively, if we actively rotate an image with a certain angle, view the rotated image, and then align the image back to the original angle, the semantics we get should be consistent with those we directly get from the un-rotated image. As shown in Fig 1, a pixel on an endoscopic image \mathcal{I} is labeled by the position \mathbf{p} , which belongs to the instrument region.

Firstly, after a *rotation* operation with the angle φ , the rotated image is given by,

$$\mathcal{I}_\varphi = \text{Rot}(\mathcal{I}; \varphi) \quad (1)$$

The pixel position \mathbf{p} is shifted by the rotation operation.

The feature extraction implemented by convolutional layers extracts the feature map \mathcal{H} from the input \mathcal{I} , which is

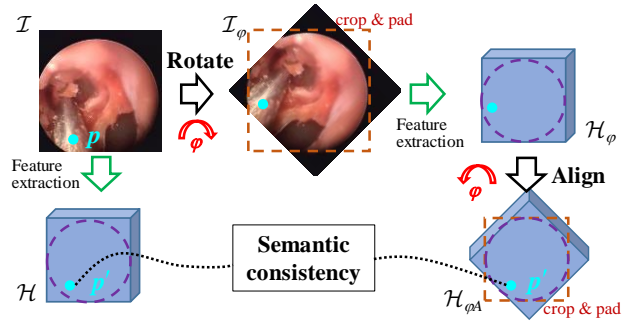


Fig. 1. Semantic consistency under rotation-and-alignment. The purple dashed circle indicates the visible circle in endoscopic image, beyond which is the black border. The cyan dot marks the same point on an instrument.

expressed as $\mathcal{H}=F(\mathcal{I})$. The rotated image \mathcal{I}_φ is input to the shared feature extraction module and converted to $\mathcal{H}_\varphi=F(\mathcal{I}_\varphi)$.

Secondly, the *alignment* operation is used to rotate \mathcal{H}_φ in the reversed direction by the same angle φ , namely,

$$\mathcal{H}_{\varphi_A} = \text{Rot}(\mathcal{H}_\varphi; -\varphi) \quad (2)$$

Thus the feature map \mathcal{H}_{φ_A} is aligned to \mathcal{H} in orientation.

The bilinear interpolation is utilized in the function $\text{Rot}()$ to allow the continuous and smooth rotation of discrete images. The image rotation relies on the cropping of out-of-field pixels and zero-padding near image corners, as is shown in Fig.1. The pixels within the visible circle of endoscope are not affected by the cropping and padding. In this paper, the rotation number was set as $N_A=4$, so that each of the four rotation angles is an integer multiple of 90° , and all the pixels are not affected by cropping and padding in rotation.

Thirdly, let \mathbf{p}' indicate the feature point on \mathcal{H} corresponding to the pixel \mathbf{p} on the raw image \mathcal{I} , the assumption of semantic consistency under rotation-and-alignment requires that the feature $\mathcal{H}_{\varphi_A}(\mathbf{p}')$ has the consistent semantics with the feature $\mathcal{H}(\mathbf{p}')$ at the same position \mathbf{p}' , although generally these two feature vectors are not equal in values. Here the semantic consistency means that the features in the same channel refer to the same attribute of object, so that they can be aggregated together in a channel-wise manner for object perception.

B. Multi-angle Feature Aggregation

We propose to generate augmented features by the rotation-and-alignment operations given one input image \mathcal{I} and multiple rotation angles $\{\varphi_k\}$, as expressed by,

$$\mathcal{H}_{\varphi_A}^{(k)} = \text{Rot}\left(F\left(\text{Rot}(\mathcal{I}; \varphi_k)\right); -\varphi_k\right) \quad (3)$$

where $k=1,2,\dots,N_A$ and N_A is the number of rotation angles. In the set $\{\mathcal{H}_{\varphi_A}^{(k)}\}$, a different $\mathcal{H}_{\varphi_A}^{(k)}$ contains the consistent semantic feature when observing the input image from a different angle φ_k .

The aggregated feature is produced by averaging the multi-angle feature maps,

$$\mathcal{H}_{MA}(i, j, c) = \frac{1}{N_A} \sum_{k=1}^{N_A} \mathcal{H}_{\varphi_A}^{(k)}(i, j, c) \quad (4)$$

where i, j and c are the indexes in height, width and channel of the feature map, respectively. The contribution of each rota-

¹<https://github.com/SURA23/Sinus-Surgery-Endoscopic-Image-Datasets>

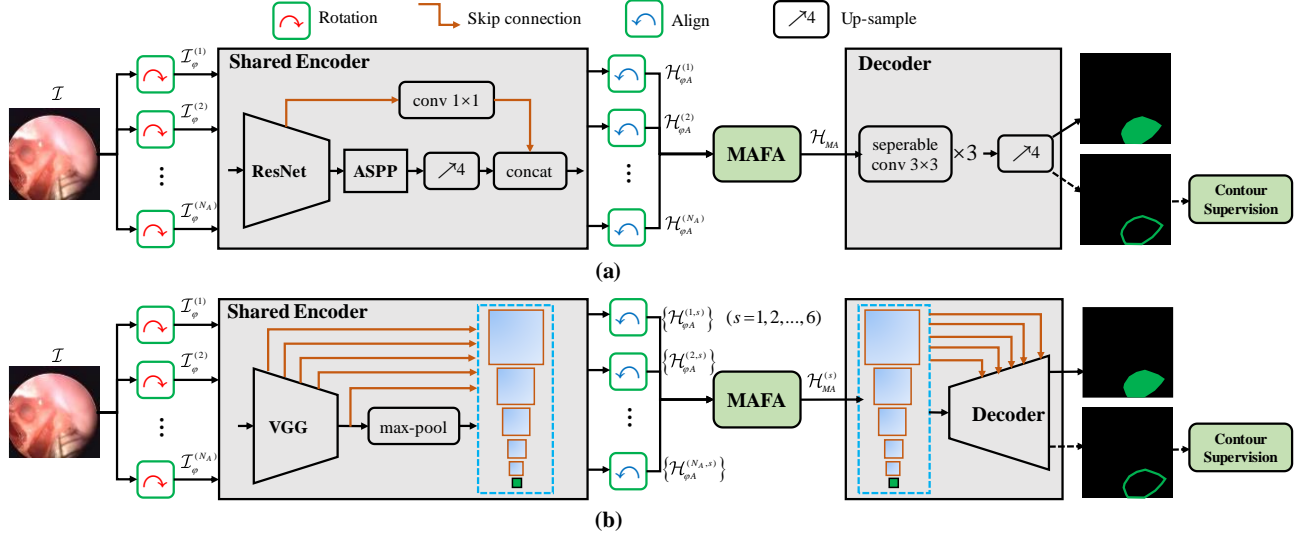


Fig. 2. Combination of MAFA and contour supervision with deep segmentation models. (a) Combine with DeepLabV3+ architecture. (b) Combine with TerausNet-16 architecture. The dashed lines before the output maps mean that the contour prediction is optionally used in the inference stage.

tion is considered the same in the averaging operation. Thus, \mathcal{H}_{MA} has the same feature channel number with $\mathcal{H}_{\phi_A}^{(k)}$ but contains the aggregated information generated by multi-angle rotation-and-alignment.

C. Contour Supervision and Loss Function

Inspired by [25], the multi-task learning supervised by both region segmentation and boundary prediction can make the model pay more attention to the object contour. The contour is informative because it not only localizes the precise edges but also represents the object's outer shape. Therefore, the final outputs of the segmentation model are two maps given by softmax function: the segmentation map \mathcal{S} and the contour map \mathcal{C} , whose sizes are the same as the input image. In our binary segmentation task, both the maps have 2 channels. The ground truth of contour map is \mathcal{C}' , obtained by finding the outer contour of the foreground regions in the ground truth of segmentation map \mathcal{S}' . The contour width is set as 2pixel.

As is different with [25], to increase contour sharpness, we use the Dice loss instead of cross-entropy loss to supervise the learning of contour prediction, as expressed by,

$$\mathcal{L}_C = 1 - \sum_{i,j,k} 2\mathcal{C}_{i,j,k}\mathcal{C}'_{i,j,k} / \left(\sum_{i,j,k} \mathcal{C}_{i,j,k}^2 + \sum_{i,j,k} \mathcal{C}'_{i,j,k}^2 + \tau \right) \quad (5)$$

where i, j and k are the indexes in height, width and channel of the output map. Here $k=1$ indicates the background probability. $k=2$ indicates the contour probability. τ is a small positive constant like $1 \times e^{-6}$ to stabilize the calculation. The segmentation learning is based on the standard cross-entropy loss,

$$\mathcal{L}_S = -\frac{1}{N} \sum_{i,j,k} \mathcal{S}'_{i,j,k} \log(\mathcal{S}_{i,j,k}) \quad (6)$$

where N is the count of all the map elements. Finally, the multi-task learning is supervised the combination of these two losses,

$$\mathcal{L} = \mathcal{L}_S + \mathcal{L}_C \quad (7)$$

III. EXAMPLES

The proposed MAFA and contour supervision methods can be flexibly combined with a segmentation model. In his section, two segmentation models, DeepLabv3+ [26] and TerausNet-16 [17], are used as examples to describe the integration of proposed methods. These two models are both based on encoder-decoder architecture, as shown in Fig. 2. The former is a typical model with spatial pyramid pooling intermedia and sparse skip connection. The latter is a typical model with the U-shape and dense skip connections.

After integrating MAFA, an input image \mathcal{I} is rotated by N_A angles, $\{\varphi_k\} = \{2\pi \times k / N_A\}$ ($k=1, 2, \dots, N_A$). All the rotated images $\mathcal{I}_{\phi}^{(k)}$ are processed by a shared encoder in parallel, thus the GPU's parallel computation advantage is leveraged. The encoder outputs are aligned to the original angle, so that the multi-angle feature maps $\mathcal{H}_{\phi_A}^{(k)}$ are produced. Then, the MAFA block fuses the multiple maps as one aggregated feature map, as is described by Eq. (4). Finally, the decoder converts the aggregated feature map to the segmentation map and contour map.

A. DeepLabv3+ with MAFA and Contour Supervision

DeepLabv3+ model is mainly characterized by its atrous spatial pyramid pooling (ASPP) block and brief structure with only one skip connection route. We customize the original DeepLabv3+ model as described below.

1) ResNet-50 [27] is used as the backbone feature extractor, outputting a feature map with 2048 channels and the 16 output-stride. *Output-stride* is the ratio of input image resolution to map resolution.

2) ASPP block is configured with four branches: an image pooling branch, a 1×1 convolution branch and two 3×3 convolution branches with the atrous rates $\{2, 4\}$. Each branch's output map has 256 channels. The four branches' outputs are concatenated in channels and then compressed as a 256-channel map by a 1×1 convolution layer.

3) The skip connection pulls out the low-level feature map, i.e. the output of the 8th layer in ResNet-50. The low-level feature map with 64 channels is adapted to 32-channel by 1×1 convolution. The 256-channel high-level feature map is resized to $4 \times$ larger with bilinear-interpolation, and concatenated with the low-level features. Thus the final encoder output is a 288-channel multi-scale feature map.

4) In the decoder, the three depthwise separable convolution layers have 3×3 kernel and 1×1 stride. The first two layers have the 128-channel outputs, and the last layer has the 4-channel output with the 4 output-stride. The first two channels are for segmentation and the last two for contour prediction. Finally, the $4 \times$ up-sampling with bilinear interpolation is used to resize the maps to the input size. Batch normalization is applied after convolutional layers to stabilize the training, and ReLUs are used for activation.

B. TerausNet-16 with MAFA and Contour Supervision

TerausNet-16 is featured by its pre-trained VGG-16 encoder and its decoder block design. The original TerausNet-16 model is combined with MAFA without customization. Because TerausNet-16 has as many as 5 skip connections, we define the encoder output as a set of 6 feature maps: one bottleneck feature map and five skipping feature maps, as shown in Fig. 2. Note that the 6 feature maps have different sizes, encoding hierarchical visual cues.

With the multi-angle rotation, the encoder outputs include $6 \times N_A$ feature maps, which are aligned to the original angle and labeled as $\{\mathcal{H}_{\varphi_A}^{(k,s)}\}$ ($k=1,2,\dots,N_A; s=1,2,\dots,6$). k and s indicate the angle index and scale index of the feature maps, respectively. MAFA block fuses the multi-angle hierarchical maps $\{\mathcal{H}_{\varphi_A}^{(k,s)}\}$ to the aggregated hierarchical maps $\{\mathcal{H}_{MA}^{(s)}\}$, which are input to the decoder in sequence. ReLUs are used for activation and softmax is used as the output function.

IV. EXPERIMENTS AND RESULTS

In the ablation experiments, we only changed whether or not to combine the proposed methods with a segmentation model, focusing on the relative performance change influenced by the proposed methods only. Thus the tedious deep learning tuning on hyper-parameters, structure details, and optimization strategy were not involved.

A. Sinus-Surgery Datasets

1) *Sinus-Surgery-C* dataset: It was collected from 10 surgeries conducted on 5 cadaver specimens. Each cadaver specimen was operated on twice, through the left and right nasal cavities, respectively. 9 surgeons participated in the experiments using the same micro-debrider surgical instrument, as is shown in Fig. 3. Each surgeon operated on one specimen, except one surgeon who operated on two. Cadaver specimens had apparent tissue color differences. Thus, the 10 videos contained diversity in both tissue backgrounds and surgical motion skills. The endoscopic videos were recorded with the 320×240 resolution and 30fps frame rate, utilizing the Stryker 1088 HD camera system and the Karl Storz Hopkins $\varnothing 4\text{mm } 0^\circ$ endoscope. The video durations ranged

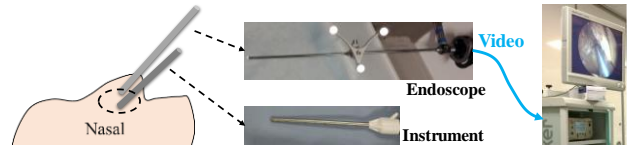


Fig. 3. Endoscopic sinus surgery schematic.

from 5 minutes to 23 minutes. The first 7 videos were used to generate the training dataset, which had 2917 images. The remaining 3 videos were used to generate the testing dataset, which had 1496 images. All the images were center-cropped to 240×240 and manually given ground truths of instrument foreground. Note that the test and training datasets were collected from different cadaver experiments, so that the generalization ability of models could be revealed.

2) *Sinus-Surgery-L* dataset: It was collected from 3 live operating room surgeries conducted on 3 patients. The total duration of the 3 endoscopic videos was about 2.5 hours. The dataset is built in a similar way with *Sinus-Surgery-C*. The training and test sets were collected from the first two and the last videos, respectively, which included 3506 and 1154 images, respectively. Compared to *Sinus-Surgery-C*, this dataset was more challenging because there were multiple instrument types, sometimes inadequate visualization and bodily secretions altering the scene.

B. Training Details

The deep models were trained with the Adam optimizer, whose exponential decay rates of the 1st and 2nd order moment estimates were 0.9 and 0.999, respectively. The training epoch and batch size were 40 and 16, respectively. The learning rate was initialized as 0.0005. The exponential decay strategy of learning rate was used, whose decay rate and step were 0.5 and 10 epochs, respectively. The backbones ResNet-50 and VGG-16 were pre-trained on ImageNet, and their outputs passed through dropout layer with 0.5 keep-rate to avoid overfitting. Data augmentation is beneficial for generalization ability. Before each optimization step, the random augmentation was applied including: hue, brightness, saturation, contrast, left-right flip, up-down flip, rotation, zoom in with random center point, zoom-out and zero-padding. Note that the random rotation angles ranged from -180° to 180° . The hardware configuration included a 3.70GHz Intel i7-8700K CPU and two Nvidia GTX2080ti GPUs.

C. Evaluation Metrics

The standard Dice similarity coefficient (DSC) and intersection of union (IOU) were used as the overall metrics,

$$\text{DSC} = \frac{2|S \cap G|}{|S| + |G|}, \text{IOU} = \frac{|S \cap G|}{|S \cup G|},$$

where $|\cdot|$ is the counting operation. S and G are the foreground pixels of the prediction and ground truth, respectively. We also used two additional metrics: *rotational standard deviation of IOUs* (RSD_{IOU}) and *IOU near boundary* (IOU_{NB}),

$$\text{RSD}_{\text{IOU}} = \text{stdev}(\{\text{IOU}_i\}_{i=1,2,\dots,6}), \text{IOU}_{\text{NB}} = \frac{|(S \cap G) \cap B|}{|(S \cup G) \cap B|},$$

TABLE I
SEGMENTATION PERFORMANCES IN ABLATION EXPERIMENTS WITH SINUS-SURGERY DATASETS

Gr.	No.	Model	Proposed		Sinus-Surgery-C				Sinus-Surgery-L				Time (ms)
			MAFA	CS	mDSC (%)	mIOU (%)	mRSD _{IOU} (%)	mIOU _{NB} (%)	mDSC (%)	mIOU (%)	mRSD _{IOU} (%)	mIOU _{NB} (%)	
1	1	DeepLabv3+ [26] with ResNet50	×	×	89.1	83.5	25.7	71.7	76.5	69.0	26.3	56.4	7
	2		×	✓	90.3	85.4	25.0	76.2	84.2	78.4	28.3	67.3	7
	3		✓	×	93.2	88.6	2.2	78.9	82.7	75.5	7.0	63.2	14
	4		✓	✓	93.9	89.5	2.3	80.2	88.1	82.8	4.6	72.1	14
2	1	TernausNet-16 [17] with VGG16	×	×	88.6	83.2	23.9	73.8	79.1	72.3	25.8	63.5	11
	2		×	✓	89.9	85.1	19.5	76.6	81.2	75.3	28.3	70.0	11
	3		✓	×	92.4	87.6	3.4	78.8	82.4	75.7	11.2	65.3	31
	4		✓	✓	93.3	88.9	3.1	81.0	84.3	78.5	8.8	68.4	31
3	1	DeepLabv3+ [26] with MobileNet	×	×	87.4	80.7	22.4	68.1	70.8	62.3	23.8	49.6	3
	2		×	✓	88.2	82.2	24.2	70.8	75.1	67.3	25.4	56.4	3
	3		✓	×	91.4	86.1	2.8	75.5	83.0	75.7	6.5	62.8	6
	4		✓	✓	93.0	88.3	2.5	78.5	83.7	76.9	6.3	64.0	6
4	1	MFF+SPP [20] with MobileNet	×	×	84.6	77.5	24.6	66.4	72.7	64.1	25.5	54.0	4
	2		×	✓	87.8	82.1	25.0	72.7	72.2	64.2	28.6	54.5	4
	3		✓	×	90.5	84.6	6.5	75.3	81.2	73.0	11.6	62.7	7
	4		✓	✓	91.2	86.4	4.7	77.8	82.6	75.1	9.2	66.8	7
5	1	LWANet [23] with MobileNet	×	×	85.2	78.1	24.8	64.8	72.3	63.2	24.7	50.0	4
	2		×	✓	86.9	81.3	31.0	72.1	77.9	69.8	30.1	60.7	4
	3		✓	×	90.1	84.5	5.1	71.9	82.1	74.6	9.9	64.2	8
	4		✓	✓	91.6	86.6	3.8	76.9	79.6	72.0	9.0	55.1	8

* The bold and italic fonts indicate the best performance in the group and in the column, respectively.

where IOU_i here is the IOU of the rotated ground truth and the prediction of the rotated input image, given the i^{th} rotation angle. The six angles are $\{0^\circ, 60^\circ, 120^\circ, 180^\circ, 240^\circ, 300^\circ\}$. The $stdev$ function is used to get the standard deviation of the set $\{IOU_i\}_{i=1,2,\dots,6}$. B denotes the near-boundary binary mask, and its foreground pixels form a 20pixel-width band region along the instrument's boundary.

Thus, RSD_{IOU} is a metric of rotation-invariance. Smaller RSD_{IOU} is better, indicating that IOU keeps more consistent under rotation. IOU_{NB} is a metric of contour accuracy. The mean values of these four metrics are calculated over all the testing examples, labeled as mDSC, mIOU, mRSD_{IOU} and mIOU_{NB}, respectively.

D. Ablation Experiments

With the Sinus-Surgery datasets, we conducted four groups of ablation experiments. Group 1 and 2 were based on the two models described in Section III. Groups 3-5 were based on three faster models re-implemented with the same backbone, i.e. the lightweight MobileNet [28] pretrained on ImageNet, considering the real-time application requirement. In Group 3, we customized the DeepLabv3+ model in Group 1 by only altered the backbone from ResNet50 to MobileNet. In Group 4, the model was featured by the multi-resolution feature fusion (MFF) and spatial pyramid pooling (SPP) [20]. The skip connection is empirically customized from sum to concatenation to improve the performance, and the adversarial learning in the original method was not used here. In Group 5, LWANet was featured by attention fusion block and depth-wise separable convolution [23]. In each group, four ablation experiments were conducted by controlling whether to use the proposed methods. The evaluation results were given in Table I.

1) *Effectiveness of MAFA*: In each group, the comparison between No. 1 and 3 showed the effectiveness of MAFA. For Sinus-Surgery-C dataset, the average improvements in the five groups were 4.5% in mDSC and 5.7% in mIOU. For Sinus-Surgery-L, the average improvements in the five groups were 8.0% in mDSC and 8.7% in mIOU. Therefore, the integration of MAFA provided a significant relative increase of segmentation accuracy.

2) *Effectiveness of contour supervision (CS)*: In each group, the comparisons between No. 1 and 2, between No. 3 and 4, presented the effectiveness of contour supervision without and with MAFA, respectively. Overall, due to contour supervision, the average improvements in the five groups were 1.4% in mDSC and 2.1% in mIOU for Sinus-Surgery-C. The average improvements in the five groups were 2.6% in mDSC and 3.5% in mIOU for Sinus-Surgery-L. Therefore, the contour supervision provided a further relative increase of segmentation accuracy, except the case in Group 5 No. 4.

3) *Influence on rotation invariance*: With the mRSD_{IOU} metric, it was shown that the rotation-invariance performances were significantly improved by MAFA, reducing mRSD_{IOU} from 19.5~31.0% down to 2.2~6.5% for Sinus-Surgery-C dataset, and from 23.8~30.1% down to 4.6~11.6% for Sinus-Surgery-L dataset. We also observed that without MAFA the rotation often caused blank output and the drop of IOU down to zero. As is shown in Fig. 4, without MAFA, the rotation might cause a large change of segmentation accuracy. For example, the TernausNet failed to recognize the instrument in the raw image of Fig. 4(b), but could recognize the instrument in the rotated image.

4) *Influence on contour awareness*: With the mIOU_{NB} metric, it was shown that the segmentation accuracy near the instrument boundary was improved by using contour super-

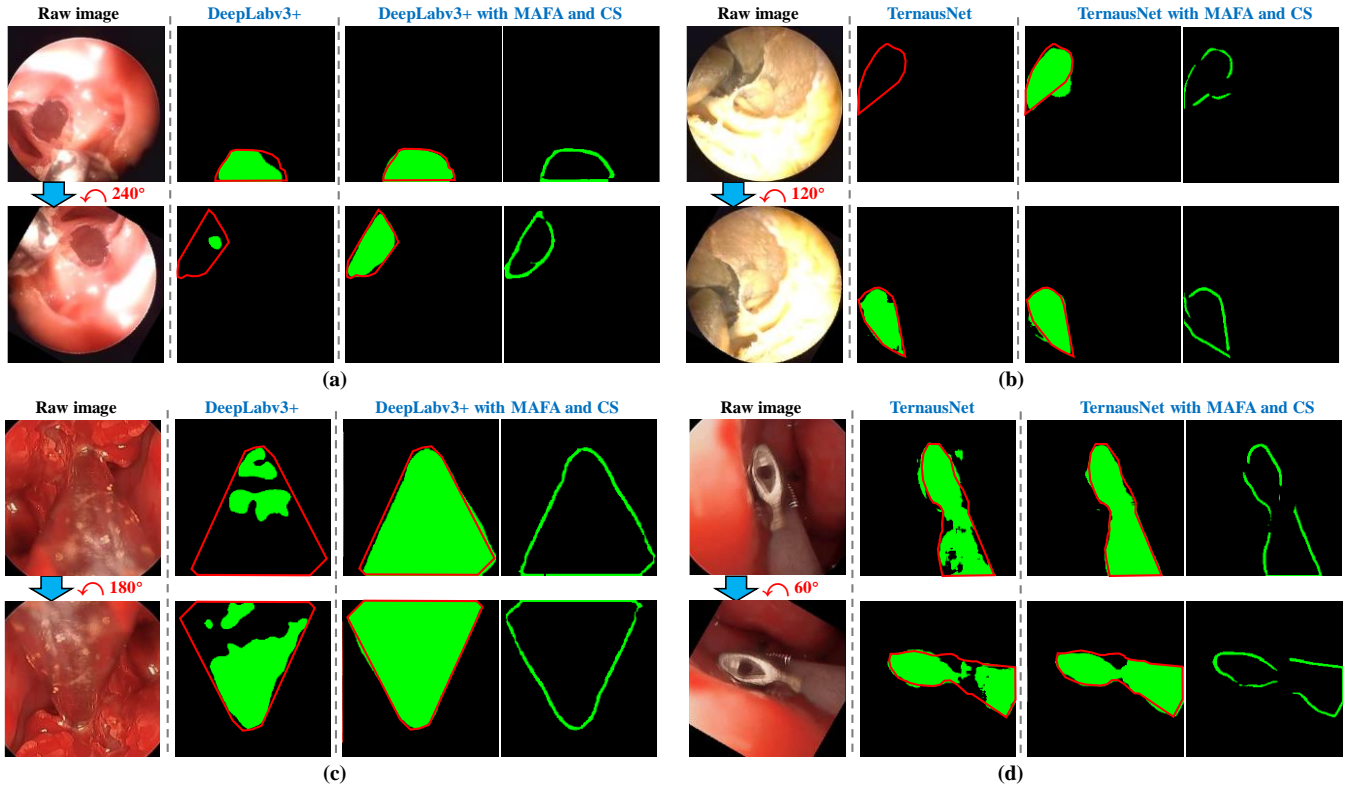


Fig. 4. Influence of image rotation on segmentation accuracy. In each sub-figure, the first and second rows correspond to the raw image input and the rotated image input, respectively. The rotation angles are labeled by red digits. (a) and (b) are from Sinus-Surgery-C dataset. (c) and (d) are from Sinus-Surgery-L dataset. The groundtruth of the foreground region is marked with red contour. The predicted foreground and contour are drawn in green.

vision. Comparing No. 2 and 4 with those of No. 1 and 3, respectively, IOU_{BN} was increased by 3.8% for Sinus-Surgery-C and by 5.6% for Sinus-Surgery-L. The contour prediction results were illustrated in Fig. 4, which showed sharpness but might have incompleteness.

4) *Influence on real-time performance*: The time costs of model inference with the 240×240 input size are also listed in Table I. The contour prediction had an ignorable influence on runtime and could be optionally unused. MAFA increased the runtime because the image number fed into feature extractor increased from 1 to $N_A=4$. Due to the GPU's parallel architecture, the time cost was doubled instead of quadrupled.

E. Discussion

MAFA provides augmented features by rotating the input image. Another way to augment features is to use a deeper and wider backbone feature extractor. First, a deeper and wider backbone will increase the parameter numbers for training but MAFA will not. Second, comparing the three lightweight models with MAFA to the other two heavier models with ResNet50/VGG16 but without MAFA, the former showed the better accuracy, and nearly the same or even faster speed. Therefore, the combination of MAFA and lighter model could surpass the heavier model with more layers and feature channels.

The contour prediction layer is a bypass of the segmentation layer. They are coupled by sharing the same input features. Therefore, although the contour supervision loss does not back-propagate through the segmentation layer, it guides the model to learn more contour aware features, which benefits the segmentation layer in an indirect manner.

V. CONCLUSION

Aiming to improve surgical instrument segmentation in challenging endoscopic images, MAFA and contour supervision are proposed to enhance a deep segmentation model. The idea of MAFA is that by actively rotating an image with multiple angles, more visual cues can be collected. The semantic consistency is assumed under rotation-and-alignment, based on which the multi-angle features can be aligned in orientation and fused by summation. For better accuracy near the instrument boundary, the sharp contour prediction is added as an auxiliary learning task to guide the model to infer boundary-aware features. The proposed method can be flexibly combined with a deep model, without increasing the parameter number. The two novel instrument segmentation datasets were collected from endoscopic sinus surgeries, which have challenges caused by dexterous motion and narrow operating space. In the future, it is appealing to leverage temporal information across multi-frames to realize robust segmentation, because it might be difficult even impossible to recognize the instrument from single frame in some cases.

VI. ACKNOWLEDGEMENTS

We are pleased to acknowledge support from National Science Foundation (grant number: IIS-1637444).

REFERENCES

- [1] B. Münzer, K. Schoeffmann, and L. Bözörmenyi, "Content-based processing and analysis of endoscopic images and videos: A survey," *Multimed. Tools Appl.*, vol. 77, no. 1, pp. 1323–1362, 2018.

- [2] S. Leonard, A. Sinha, A. Reiter, *et al.*, "Evaluation and stability analysis of video-based navigation system for functional endoscopic sinus surgery on in-vivo clinical data," *IEEE Trans. Med. Imag.*, vol. 37, no. 10, pp. 2185-2195, 2018.
- [3] N. Mahmoud, T. Collins, A. Hostettler, *et al.*, "Live tracking and dense reconstruction for handheld monocular endoscopy," *IEEE Trans. Med. Imag.*, vol. 38, no.1, pp. 79-89, 2019.
- [4] G. A. Puerto-Souza, J. A. Cadeddu, and G. Mariottini, "Toward long-term and accurate augmented-reality for monocular endoscopic videos," *IEEE Trans. Biomed. Eng.*, vol. 61, no. 10, pp. 2609-2620, 2014.
- [5] A. Jin, S. Yeung, J. Jopling, *et al.*, "Tool detection and operative skill assessment in surgical videos using region-based convolutional neural networks," in *Proc. IEEE Winter Conf. Appl. Comput. Vis.*, pp. 691-699, 2018.
- [6] R. H. Taylor and D. Stoianovici, "Medical robotics in computer-integrated surgery," *IEEE Trans. Robot. Autom.*, vol. 19, no. 5, pp.765-781, 2003.
- [7] B. Hannaford, J. Rosen, D. W. Friedman, *et al.*, "Raven-II: an open platform for surgical robotics research," *IEEE Trans. Biomed. Eng.*, vol. 60, no. 4, pp. 954-959, 2013.
- [8] D. Hu, Y. Gong, E. J. Seibel, *et al.*, "Semi-autonomous image-guided brain tumor resection using an integrated robotic system: A bench-top study," *Int. J. Med. Robot. Comput. Assist. Surg.*, vol. 14, no. 1, pp. e1872, 2018.
- [9] M. Ye, L. Zhang, S. Giannarou, *et al.*, "Real-time 3d tracking of articulated tools for robotic surgery," in *Proc. Int. Conf. Med. Image Comput. Comput. Assist. Interv.*, pp. 386-394, 2016.
- [10] D. Bouget, M. Allan, D. Stoyanov, *et al.*, "Vision-based and marker-less surgical tool detection and tracking: a review of the literature," *Medical Image Analysis*, vol. 35, pp.633-654, 2017.
- [11] L. C. Garcia-Peraza-Herrera, W. Li, L. Fidon, *et al.*, "ToolNet: holistically-nested real-time segmentation of robotic surgical tools," in *Proc. IEEE Int. Conf. Intell. Robot. Syst.*, 2017, pp. 5717-5722.
- [12] J. Long, E. Shelhamer, and T. Darrell, "Fully convolutional networks for semantic segmentation," in *Proc. IEEE Conf. Comput. Vis. Pattern Recognit.*, pp. 3431-3440, 2015.
- [13] I. Laina, N. Rieke, C. Rupprecht, *et al.*, "Concurrent segmentation and localization for tracking of surgical instruments," in *Proc. Conf. Med. Image Comput. Comput. Assist. Interv.*, 2017, pp. 664-672.
- [14] M. Attia, M. Hossny, S. Nahavandi, *et al.*, "Surgical tool segmentation using a hybrid deep CNN-RNN auto encoder-decoder," in *Proc. IEEE Int. Conf. Syst. Man Cybern.*, 2017, pp.3373-3378.
- [15] F. Qin, Y. Li, Y. H. Su, *et al.*, "Surgical instrument segmentation for endoscopic vision with data fusion of CNN prediction and kinematic pose," in *Proc. Int. Conf. Robot. Autom.*, pp. 9821-9827, 2019.
- [16] O. Ronneberger, P. Fischer, and T. Brox, "U-Net: Convolutional networks for biomedical image segmentation," in *Proc. Int. Conf. Med. Image Comput. Comput. Assist. Interv.*, pp. 234-241, 2015.
- [17] A. Shvets, A. Rakhlin, A. A. Kalinin, *et al.*, "Automatic instrument segmentation in robot-assisted surgery using deep learning," in *Proc. IEEE Int. Conf. Mach. Learn. Appl.*, pp. 624-628, 2018.
- [18] A. Chaurasia and E. Culurciello, "Linknet: Exploiting encoder representations for efficient semantic segmentation," in *Proc. IEEE Visual Commun. Image Process.*, pp. 1-4, 2017.
- [19] V. Iglovikov and A. Shvets, "TernausNet: U-Net with VGG11 encoder pretrained on imagenet for image segmentation," arXiv:1801.05746, 2018.
- [20] M. Islam, D. A. Atputharuban, R. Ramesh, *et al.*, "Real-time instrument segmentation in robotic surgery using auxiliary supervised deep adversarial learning," *IEEE Robot. Autom. Lett.*, vol. 4, no. 2, pp. 2188-2195, 2019.
- [21] H. Zhao, J. Shi, X. Qi, *et al.*, "Pyramid scene parsing network," in *Proc. IEEE Conf. Comput. Vis. Pattern Recognit.*, pp. 2881-2890, 2017.
- [22] H. Zhao, X. Qi, X. Shen, *et al.*, "ICNet for real-time semantic segmentation on high-resolution images," in *Proc. Europ. Conf. Comput. Vis.*, pp. 405-420, 2018.
- [23] Z. Ni, G. Bian, Z. Hou, *et al.* "Attention-guided lightweight network for real-time segmentation of robotic surgical instruments," in *Proc. Int. Conf. Robot. Autom.*, accepted, 2020. (online available: arXiv preprint arXiv:1910.11109)
- [24] Y. Jin, K. Cheng, Q. Dou, *et al.*, "Incorporating temporal prior from motion flow for instrument segmentation in minimally invasive surgery video," in *Proc. Int. Conf. Med. Image Comput. Comput. Assist. Interv.*, pp: 440-448, 2019.
- [25] H. Si, Z. Zhang, F. Lv, *et al.*, "Real-time semantic segmentation via multiply spatial fusion network," *arXiv preprint arXiv:1911.07217*, 2019.
- [26] L. C. Chen, Y. Zhu, G. Papandreou, *et al.*, "Encoder-decoder with atrous separable convolution for semantic image segmentation," in *Proc. Europ. Conf. Comput. Vis.*, pp. 801-818, 2018.
- [27] K. He, X. Zhang, S. Ren, *et al.*, "Identity mappings in deep residual networks," in *Proc. Europ. Conf. Comput. Vis.*, pp. 630-645, 2016.
- [28] A. G. Howard, M. Zhu, B. Chen, *et al.*, "MobileNets: Efficient convolutional neural networks for mobile vision applications," *arXiv preprint arXiv:1704.04861*, 2017.